Characterization and catalytic activity of soft-templated NiO-CeO2 mixed oxides for CO and CO2 co-methanation

Front. Chem. Sci. Eng. 2021, 15(2): 251–268
https://doi.org/10.1007/s11705-020-1951-8

RESEARCH ARTICLE

Characterization and catalytic activity of soft-templated NiO-CeO_2 mixed oxides for CO and CO_2 co-methanation

Luciano Atzori[1], Maria Giorgia Cutrufello[1], Daniela Meloni[1], Barbara Onida[2], Delia Gazzoli[3], Andrea Ardu[1], Roberto Monaci[1], Maria Franca Sini[1], Elisabetta Rombi (✉)[1]

1 Department of Chemical and Geological Sciences, University of Cagliari, 09042 Monserrato (CA), Italy
2 Department of Materials Science and Chemical Engineering, CR-INSTM for Materials with Controlled Porosity, Polytechnic of Turin, 10129 Turin, Italy
3 Department of Chemistry, University of Rome "La Sapienza", 00185 Rome, Italy

Abstract Nanosized NiO, CeO_2 and NiO-CeO_2 mixed oxides with different Ni/Ce molar ratios were prepared by the soft template method. All the samples were characterized by different techniques as to their chemical composition, structure, morphology and texture. On the catalysts submitted to the same reduction pretreatment adopted for the activity tests the surface basic properties and specific metal surface area were also determined. NiO and CeO_2 nanocrystals of about 4 nm in size were obtained, regardless of the Ni/Ce molar ratio. The Raman and X-ray photoelectron spectroscopy results proved the formation of defective sites at the NiO-CeO_2 interface, where Ni species are in strong interaction with the support. The microcalorimetric and Fourier transform infrared analyses of the reduced samples highlighted that, unlike metallic nickel, CeO_2 is able to effectively adsorb CO_2, forming carbonates and hydrogen carbonates. After reduction in H_2 at 400 °C for 1 h, the catalytic performance was studied in the CO and CO_2 co-methanation reaction. Catalytic tests were performed at atmospheric pressure and 300 °C, using $CO/CO_2/H_2$ molar compositions of 1/1/7 or 1/1/5, and space velocities equal to 72000 or 450000 $cm^3 \cdot h^{-1} \cdot g_{cat}^{-1}$. Whereas CO was almost completely hydrogenated in any investigated experimental conditions, CO_2 conversion was strongly affected by both the $CO/CO_2/H_2$ ratio and the space velocity. The faster and definitely preferred CO hydrogenation was explained in the light of the different mechanisms of CO and CO_2 methanation. On a selected sample, the influence of the reaction temperature and of a higher number of space velocity values, as well as the stability, were also studied. Provided that the Ni content is optimized, the NiCe system investigated was very promising, being highly active for the CO_x co-methanation reaction in a wide range of operating conditions and stable (up to 50 h) also when submitted to thermal stress.

Keywords soft template method, NiO-CeO_2 catalysts, CO and CO_2 co-methanation, synthetic natural gas production

1 Introduction

Several studies have clearly demonstrated the connection between the greenhouse gases (GHGs) emissions and the climate system [1]. Carbon dioxide is estimated to account for 77% of GHGs emissions and is thus considered as the main cause of climate change. The major contribution to such a massive emission of CO_2 can be associated with the use of carbon-based fuels that currently provide about 80%–85% of the global total primary energy supply [2,3]. CO_2 concentration is also expected to increase in the next decades, especially because of the robust economic growth of emerging countries, such as China and India. The energy structure of these countries is dominated by coal, which is the most environmentally impacting raw material, since its combustion produces the highest CO_2 amount per unit of heat compared to the other carbon-based fuels [4,5]. However, contrary to both oil and natural gas, whose reserves are expected to be depleted in the next few decades, coal availability is estimated to last for more than 150 years. In light of this, the production of synthetic natural gas (SNG) through coal gasification into syngas and its subsequent transformation into methane has attracted increasing attention. In addition, syngas can also be derived from gasification of biomass, which is a renewable source. Thus, the production of CH_4 through

Received March 28, 2019; accepted April 22, 2019

E-mail: rombi@unica.it

CO or CO_2 hydrogenation, known as the "Sabatier" or "methanation" reaction (Scheme 1), can be considered a promising alternative for the reduction of GHGs emissions as well as for a sustainable exploitation of coal reserves, especially if hydrogen is produced using renewable resources and energy. Moreover, carbon oxides methanation allows H_2 to be transformed into a substance compatible with the current technologies, since methane could be injected directly into the already existing pipeline networks or storage infrastructures.

$$CO + 3H_2 \leftrightarrows CH_4 + H_2O \quad \Delta H = -206.1 \text{ kJ·mol}^{-1}$$
$$CO_2 + 4H_2 \leftrightarrows CH_4 + 2H_2O \quad \Delta H = -165.0 \text{ kJ·mol}^{-1}$$

Scheme 1 Stoichiometric equations for CO and CO_2 hydrogenation to methane.

The methanation reactions of CO [6,7] and CO_2 [6,8] have been extensively studied on supported noble (e.g., Ru, Rh) and non-noble (Ni, Co, Fe) metals, using a wide variety of metal oxides carriers prepared with different procedures, also in the presence of promoters. Among the non-noble metals, Ni has been mainly investigated, due to its low cost, high activity and high methane selectivity. On the other hand, thanks to its peculiar oxygen storage and redox properties and to the presence of oxygen vacancies in a wide range of conditions, the use of cerium oxide as a support or promoter has also been widely reported in the literature. Several papers can be found in which CeO_2-supported Ni catalysts have been used for separately converting either CO [9–13] or CO_2 [13–18] into methane.

CO methanation in the presence of different amounts of CO_2 is a well-known process for purifying H_2 streams from low CO contents (as, for example, purification of H_2 for NH_3 production or for Fuel Cells applications). Several publications regarding the selective methanation of CO in CO_2-rich reformate gas streams over NiO-CeO_2 systems also exist [19–24]. However, to the best of the present authors knowledge, only few papers [25–36] about CO and CO_2 co-methanation for SNG production have been published so far, among which five deal with catalysts based on Ni supported on CeO_2-containing carriers [29,30,32,35,36].

In this work, the co-methanation of CO and CO_2 was studied on soft-templated NiO-CeO_2 mixed oxides catalysts with different Ni/Ce molar ratios (0.3–4.0). The synthesized samples were characterized by different techniques as to their chemical composition, structure, morphology, and texture. On the catalysts submitted to the same reduction pretreatment adopted for the activity tests the surface basic properties and specific metal surface area were also determined. The reaction was performed in a fixed-bed continuous-flow quartz-glass microreactor, at atmospheric pressure and 300 °C, with $CO/CO_2/H_2$ molar compositions equal to 1/1/7 or 1/1/5, and space velocities (*SV*) of 72000 or 450000 $cm^3 \cdot h^{-1} \cdot g_{cat}^{-1}$. Furthermore, on a selected sample, the effect of reaction temperature and the influence of *SV*, as well as the stability, were also investigated.

2 Experimental

2.1 Materials

Cetyltrimethyl-ammonium bromide (CTAB,≥98%), $Ni(NO_3)_2 \cdot 6H_2O$ (99.999%), $Ce(NO_3)_3 \cdot 6H_2O$ (99%), and NaOH (pellets, 97%) were supplied by Aldrich. Ethanol (96%) was supplied by Fluka. HCl (37%) was provided by Merck. The gaseous feed mixture with known concentration of the components was supplied by SAPIO.

2.2 Synthesis of catalysts

NiO-CeO_2 mixed oxides with Ni/Ce molar ratios in the range 0.3–4.0 were synthesized through the soft template method [37,38], using $Ce(NO_3)_3 \cdot 6H_2O$ and $Ni(NO_3)_2 \cdot 6H_2O$ as cerium and nickel oxides precursors, CTAB as the template, and NaOH as the precipitating agent. For the synthesis, appropriate amounts of the nitrate precursors and the template (CTAB/precursors = 0.62 $mol \cdot mol^{-1}$) were dissolved at room temperature in 100 cm^3 of distilled water under stirring. After 30 min, a 0.17 $mol \cdot L^{-1}$ solution of NaOH was added dropwise until a pH value of 13 was reached; the mixture was then stirred for 15 h. After digestion at 90 °C for 3 h, the solid formed was recovered by filtration and washed with hot distilled water (70 °C) until the formation of AgBr precipitate in the filtrate by reaction of bromides with $AgNO_3$ was no longer observed. Then, it was dried at 110 °C for 6 h and finally calcined at 450 °C for 4 h. The materials obtained were named *x*NiCe, were *x* represents the nominal value of the Ni/Ce molar ratio.

2.3 Characterization of catalysts

Transmission electron microscopy (TEM) images were obtained with a JEOL 200CX instrument. A JEOL JEM 2010 UHR microscope, equipped with a Gatan imaging filter with a 15 eV window and a 794 slow scan CCD camera, was instead used to collect high resolution TEM (HRTEM) micrographs. Both instruments operated at 200 kV. Finely ground samples were dispersed in *n*-octane in an ultrasonic bath. The suspension was then dropped onto a copper grid covered with a carbon thin film for the observation.

Raman spectra were collected at room temperature in back-scattering geometry with an inVia Renishaw micro-Raman spectrometer equipped with an air-cooled charge coupled device detector and edge filters. A 488.0 nm

emission line from an Ar ion laser was focused on the sample under a Leica DLML microscope, using 20× or 5× objectives. The power of the incident beam was about 5 mW. Repeated (10 or 20 s) accumulations were generally acquired for each sample. The resolution was 2 cm^{-1} and spectra were calibrated using the 520.5 cm^{-1} line of a silicon wafer. Spectra processing included baseline removal and curve fitting using a Gauss-Lorentz cross-product function by Peakfit 4.12 software (Jandel, AISN Software).

X-ray photoelectron spectroscopy (XPS) analysis was performed using a PHI 5000 VersaProbe scanning instrument equipped with a monochromatic Al-Kα X-ray source (1486.6 eV, 15 kV, 1 mA) and a combined electron and argon ion gun neutralizer system to reduce charging effects. C1s, O1s, Ce3d and Ni2p regions were acquired in FAT mode (23.5 eV), setting C1s at 284.7 eV. Data analysis involved smoothing, non-linear Shirley-type background subtraction, curve fitting (mixed Gaussian-Lorentzian function by a least-square method), and peak area determination by integration of the appropriate signal after data analysis (Esca Tools 4.2 software, Surface Interface Inc., Mountain View, CA). The shapes of the Ce3d and Ni2p signals were analyzed by a curve fitting procedure with Ce3d and Ni2p doublets endowed with fixed spectroscopic parameters, but using variable position, full width at half maximum, and intensity. The surface composition was determined from the peak area ratios using the empirically derived atomic sensitivity factors reported by Wagner et al. [39].

Microcalorimetric measurements were performed with a Tian-Calvet heat flow microcalorimeter (Setaram), equipped with a volumetric vacuum line. Each sample (0.1 g, 40–80 mesh), previously reduced under flowing pure H_2 (15 $cm^3 \cdot min^{-1}$) at 400 °C for 1 h, was thermally pretreated at 250 °C for 12 h under vacuum (5×10^{-3} Pa). Adsorption was carried out by admitting successive doses of the probe gas (CO_2) at 80 °C in order to limit physisorption. The equilibrium pressure relative to each adsorbed amount was measured by means of a differential pressure gauge (Datameritics) and the thermal effect was recorded. The run was stopped at a final equilibrium pressure of about 133 Pa. After outgassing overnight at the same temperature, a second adsorption run was carried out in order to calculate the amount of the probe gas irreversibly adsorbed.

Fourier transform infrared (FTIR) spectra were collected on an EQUINOX 55 spectrometer (Bruker), equipped with a MCT cryodetector working at 2 cm^{-1} resolution. Prior to FTIR measurements, thin self-supporting wafers were outgassed at 400 °C in dynamic vacuum (residual pressure $< 1\times10^{-1}$ Pa) and then exposed to H_2 (1.5×10^4 Pa) at the same temperature for 1 h. After cooling to room temperature under Ar atmosphere and outgassing to 1×10^{-1} Pa, successive doses of CO_2 were admitted and a first FTIR spectrum was collected after the equilibrium pressure of 5×10^3 Pa was reached; then, a second spectrum was recorded after outgassing for 30 min at the same temperature.

The specific surface areas of the Ni^0 metal particles were calculated by means of hydrogen temperature programmed desorption (H_2-TPD) measurements performed after H_2-pulse chemisorption runs, both carried out in a TPD/R/O 1100 apparatus (ThermoQuest). Before analysis, the sample (0.050 g) was reduced under H_2 flow (15 $cm^3 \cdot min^{-1}$) at 400 °C for 1 h. Then, N_2 (20 $cm^3 \cdot min^{-1}$) was used for purging (1 h) and cooling to 50 °C. Pulses of H_2 (5 vol-% in N_2) were then admitted into the reactor until the area of the peaks remained constant. Finally, TPD analysis was carried out under flowing N_2 (20 $cm^3 \cdot min^{-1}$) while heating (10 °C $\cdot min^{-1}$) from 50 °C to 500 °C (held for 30 min). The specific metal surface area was then automatically computed by the instrument software from the desorption profile assuming a H/Ni stoichiometric factor equal to 1. Calibration of the H_2 amount evolved was previously carried out by using a copper oxide standard.

CO-TPD analyses were performed after CO-pulse chemisorption runs by means of the TPD/R/O 1100 instrument. After the sample (0.050 g) reduction under pure H_2 (15 $cm^3 \cdot min^{-1}$) at 400 °C for 1 h, pulses of CO (5 vol-% in He) were sent until the peaks area remained constant. Then, CO-TPD analyses were carried out under flowing He (20 $cm^3 \cdot min^{-1}$) while heating (10 °C $\cdot min^{-1}$) from 50 °C to 800 °C. Desorption profiles were collected by a mass spectrometer detector, through which CO and CO_2 were monitored.

Elemental analysis was carried out with an EA 1110 CHNS-O analyzer (CE Instruments) by total combustion of the samples in a mixture of oxygen and helium.

Thermogravimetric analyses (TGA) were carried out on a Perkin-Elmer STA6000 thermal analyser. The samples were placed in an alumina pan and heated under oxygen flow (20 $cm^3 \cdot min^{-1}$) from 25 °C to 850 °C (heating rate, 10 °C $\cdot min^{-1}$).

2.4 CO_2 and CO co-methanation

Typical CO and CO_2 co-methanation tests were carried out for 6 h at atmospheric pressure and 300 °C in a tubular (ϕ_{int} = 0.8 cm) quartz-glass fixed-bed continuous-flow microreactor. The reactor is provided with an external jacket containing a fluidized bed of silicon carbide, which allows keeping the system in isothermal conditions once the reaction temperature has been reached upon heating in an electric furnace. The temperature was monitored by a K-type thermocouple located in the thermostatic jacket and connected to a temperature-programmer/controller. A second K-type thermocouple was positioned inside the reactor to check the temperature of the catalytic bed (differences between the setpoint and the detected temperature values were never observed). Prior to the

reaction, the catalysts were pretreated in air (30 $cm^3 \cdot min^{-1}$) at 400 °C overnight; after purging in He (30 $cm^3 \cdot min^{-1}$), they were subsequently reduced under H_2 flow (15 $cm^3 \cdot min^{-1}$) at the same temperature for 1 h and then cooled in He (30 $cm^3 \cdot min^{-1}$) to the reaction temperature. CO and CO_2 co-methanation tests were performed with 0.050 g of catalyst by using a $CO/CO_2/H_2$ reactant gas mixture with a molar composition equal to 1/1/7 (CO, 9.5 mol-%; CO_2, 9.8 mol-%; H_2, 73.9 mol-%; N_2, used as the internal standard, 6.8 mol-%) or 1/1/5 (CO, 12.7 mol-%; CO_2, 13.2 mol-%; H_2, 64.9 mol-%; N_2, used as the internal standard, 9.2 mol-%). Two *SV*s, 72000 and 450000 $cm^3 \cdot h^{-1} \cdot g_{cat}^{-1}$, were investigated, corresponding to a total flow rate of 60 and 150 $cm^3 \cdot min^{-1}$, respectively. After 1 h on stream, online analysis of the reactor effluent was performed every hour on a 6890 (Agilent) gas chromatograph (GC), equipped with a Carboxen 1010 PLOT capillary column and a thermal conductivity detector. Water was removed from the reaction mixture through an ice trap and a molecular sieves trap placed between the reactor outlet and the GC injection valve. The results of the quantitative analysis of the carbon-containing components were used for checking the carbon mass balance and for calculating CO_x conversion and products selectivity. On the 1.0NiCe sample, the influence of the reaction temperature (from 200 °C to 400 °C) and of a wide range of space velocity (from 48000 to 450000 $cm^3 \cdot h^{-1} \cdot g_{cat}^{-1}$) was investigated. Long-time runs were also performed at different temperature ranges to study the catalytic stability under thermal stress. In addition, on the 0.3NiCe and 1.0NiCe samples, CO methanation tests at 300 °C, $H_2/CO = 3$, and $SV = 72000$ or 450000 $cm^3 \cdot h^{-1} \cdot g_{cat}^{-1}$ were carried out in order to get information on the occurrence of side-reactions possibly responsible for carbon residues formation.

3 Results and discussion

3.1 Characterization

The compositional, textural, and structural characterization of the *x*NiCe samples has already been reported and discussed in a previous work [17]. However, for the sake of clarity, the results are summarized in Table 1 and the X-ray diffraction (XRD) patterns of the present samples collected before and after the H_2-pretreatment are also shown in Fig. S1 (cf. Electronic Supplementary Material, ESM).

TEM analysis was performed on the 1.0NiCe sample before and after the H_2-pretreatment as well as after the catalytic reaction and the results are reported in Fig. 1. TEM micrographs of cerium and nickel pure oxides are shown in Figs. S2 and S3 (cf. ESM) for comparison. In agreement with previous results on NiCe samples with different Ni/Ce molar ratios [17], the TEM micrograph of the starting 1.0NiCe sample (Fig. 1(a)) shows the presence of CeO_2 (black arrows), in the form either of small, roughly spheroidal and hexagonal, nanoparticles of 3 to 5 nm in size or of thin nanofilaments (3–4 nm in diameter and up to 200 nm in length) (see also Fig. S2). Elongated nanoparticles (white arrows) are also visible, which are ascribable to NiO in the form of nanorods of 3–4 nm in diameter and 10–40 nm in length (see also Fig. S3). The comparison of these values with the average size of crystallites estimated by XRD data (i.e., around 3 and 4 nm for CeO_2 and NiO, respectively) suggests that both the nanofilaments and the nanorods could be composed of chains of small spheroidal nanocrystals, possibly because a self-organizing mechanism is established during the synthesis in the presence of the ionic surfactant (CTAB). The presence of CeO_2 and NiO in close contact is clearly evidenced by the HRTEM image in Fig. 1(b) (see also Fig. S4 (cf. ESM)), where d-spacings of 3.12 and 2.41 Å, corresponding to the (111) planes of CeO_2 and NiO, respectively, were measured on the rounded and the elongated nanocrystals. As expected, in the HRTEM image of the sample after the H_2-pretreatment (Fig. 1(c)) CeO_2 and Ni^0 nanocrystals are present (for the latter the d-spacing of the (111) plane is 2.03 Å). Noteworthy, though not observable in the relevant XRD pattern (Fig. S1(b)), the existence of residual NiO on the reduced catalyst is indicated by the detection of crystallites with d-spacing of 2.41 Å. The presence of NiO was also evidenced in the XRD patterns of 2.5NiCe and 4.0NiCe by the appearance

Table 1 Chemical composition and structural and textural features of the *x*NiCe samples and of the CeO_2 and NiO pure oxides (from ref. 17)

Sample	Ni/Ce [a] molar ratio	g_{Ni}/g_{CeO2} [a]/wt-%	Average crystallite size [b]/nm			S_{BET} [c]/($m^2 \cdot g^{-1}$)	V_p [c]/($cm^3 \cdot g^{-1}$)
			CeO_2	NiO	Ni^0		
CeO_2	–	–	5	–	–	191	0.36
0.3NiCe	0.29	9.8	3	4	n.d.	174	0.17
1.0NiCe	0.96	32.6	3	4	6	206	0.29
2.5NiCe	2.50	85.2	3	4	8	208	0.37
4.0NiCe	3.84	131.0	3	4	8	209	0.38
NiO	–	–	–	3	7	209	0.31

a) determined by inductively coupled plasma-atomic emission spectrometry (ICP-AES) analyses; b) determined by applying the Scherrer Equation [40] to the XRD data (Fig. S1) of the samples before (CeO_2 and NiO) and after (Ni^0) the H_2-pretreatment; c) determined by the N_2 adsorption/desorption isotherms. Surface area (S_{BET}) values were calculated by using the Brunner-Emmett-Teller (BET) method [41].

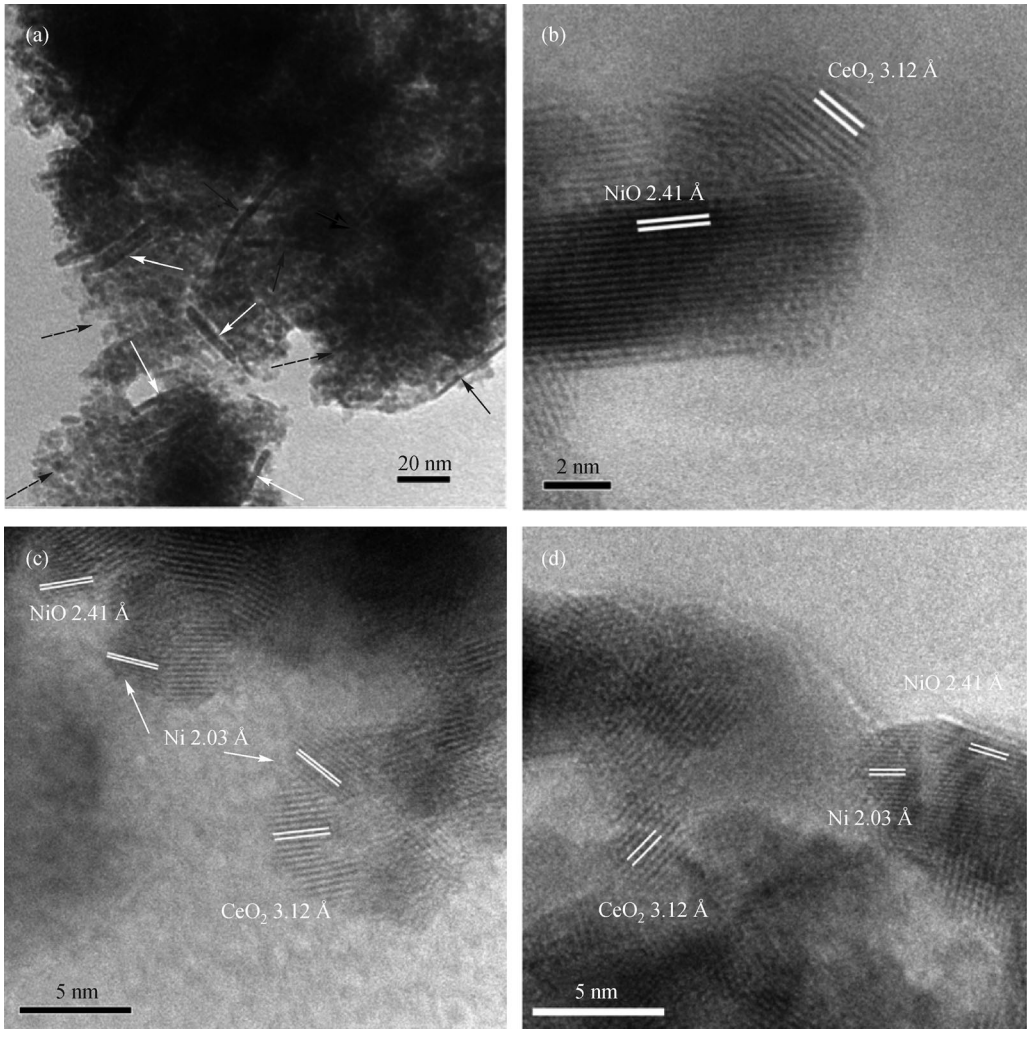

Fig. 1 (a) TEM and (b–d) HRTEM images of the 1.0NiCe sample (b) in the original oxidized form, (c) after the H_2-pretreatment at 400 °C for 1 h and (d) after reaction.

of weak and broad signals at 2θ values of 37.3°, 43.3° and 62.9° (Fig. S1(b)), supporting the view of an incomplete reduction of the starting NiO crystallites, at least for Ni/Ce molar ratios ≥1. The micrograph of the post-reaction 1.0NiCe catalyst (Fig. 1(d)) is very similar to that of the fresh one, suggesting that both the nature and the size of the Ni species are not modified during the co-methanation reaction.

The Raman spectra of the *x*NiCe samples are compared in Fig. 2, where the spectrum of a soft-templated pure cerium oxide is also reported. Pure CeO_2 shows a predominant band centered at 460 cm^{-1} (F_{2g} mode of the CeO_2 fluorite phase) and weak bands at 258, 595 and 1179 cm^{-1}, due to second-order transverse acoustic (2TA) mode, defect-induced (D) mode, and second-order longitudinal optical (2LO) mode, respectively [42–44]. All the *x*NiCe samples show Raman spectra with main features at about 440 cm^{-1} (F_{2g} mode), 578 cm^{-1} (D mode), and in the range 1080–1180 cm^{-1} in which both the 2LO mode of CeO_2 and the 2TO mode (2P) of NiO [45] are expected. Compared to the CeO_2 spectral shape, the F_{2g} mode of the *x*NiCe system shifts to lower wavenumbers at increasing Ni amounts, and both the features at about 578 cm^{-1} and in the range 1080–1180 cm^{-1} increase in intensity. The shift of the F_{2g} mode indicates a strong interaction between the NiO and CeO_2 species, with a consequent weakening of the Ce–O bond. The increase in intensity along with the Ni content of the band at about 578 cm^{-1}, which encloses contributions at about 560 cm^{-1}, due to oxygen vacancies (D_1), and at about 600 cm^{-1}, due to cation substitution in the lattice (D_2), supports the hypothesis of the formation of a solid solution [44,46]. The presence of NiO nanocrystals is clearly evidenced by the band at about 1090 cm^{-1}, which partially overlaps the 2TA mode of CeO_2 at about 1179 cm^{-1} and becomes a prominent feature with increasing Ni content.

The reduction treatment in H_2 slightly downshifts the position of the CeO_2 bands (Fig. 3(a), black curve) with

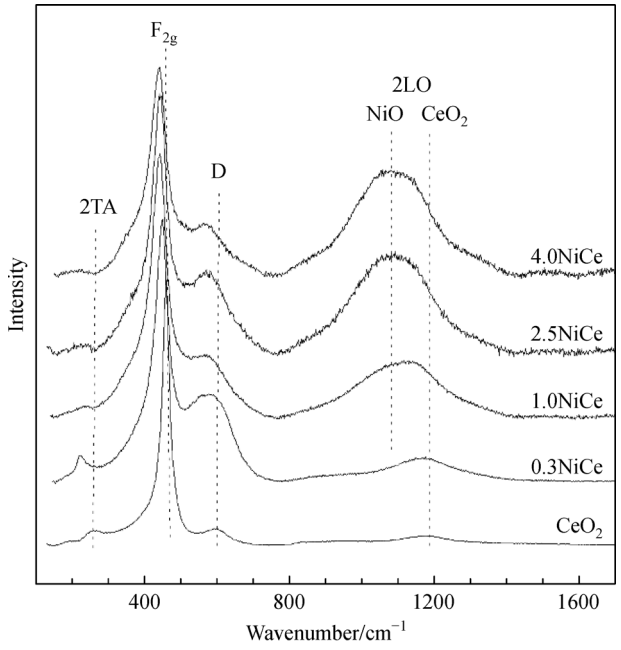

Fig. 2 Raman spectra of CeO_2 and *x*NiCe samples.

respect to the oxidized sample (Fig. 3(a), grey curve) and causes a little broadening of the F_{2g} band and a small variation in the intensity of the D band. These small changes, evidenced by the spectral profile obtained after subtracting the spectrum before H_2-pretratment from that after H_2-pretratment (Fig. 3(a), dashed curve), indicate a small reduction extent of CeO_2 [43,47], which influences the Ce–O bond strength and the defectivity. As for the 0.3NiCe sample, after the H_2-pretreatment (Fig. 3(b), black curve) both the F_{2g} and the D bands result a little broadened and red-shifted compared to those of the starting material, which are positioned at about 455 and 580 cm^{-1}, respectively (Fig. 3(b), grey curve). The difference spectrum (Fig. 3(b), dashed curve) shows the appearance of components at about 440 and 550 cm^{-1} due to a decrease in particle size (F_{2g} mode) and increase in defects (D band) because of the reduction process. Conversely, the H_2-treatment significantly modifies the Raman spectrum of the 4.0NiCe sample (Fig. 3(c)). The spectral trace resulting from the difference between spectra after and before H_2-pretreatment (Fig. 3(c), dashed curve) shows a strong decrease in the intensity of the signals at about 422 and 1080 cm^{-1} and a parallel increase in the intensity of those located at about 453 and 605 cm^{-1}. The strong decrease in intensity of the band at about 1080 cm^{-1}, associated with the 2TO mode (2P) of NiO, clearly indicates the reduction of segregated NiO species to Ni^0. The positive shift of the F_{2g} mode to about 453 cm^{-1} together with the increased D contribution at about 605 cm^{-1} suggest a structural rearrangement caused by the reduction process involving both CeO_2 and NiO species. Since the defect-induced mode (D) encloses contributions due to oxygen vacancies (at about 560 cm^{-1}) and to cation substitution in the lattice (at about 600 cm^{-1}), the higher concentration of defects could result from both the loss of oxygen and the vacancies left by the reduction of incorporated nickel ions.

The XPS analysis allowed the determination of the surface composition of the samples and a better understanding of the nature of the interactions between Ni species and cerium oxide by following the changes in the Ce3d, Ni2p and O1s features. The Ce3d spectrum (Fig. S5(a), cf. ESM)) shows a complex feature due to a satellite structure resulting from hybridization with O2p orbitals and partial occupancy of the 4f levels. According to Burroughs et al. [48] the $3d_{5/2}$ and $3d_{3/2}$ spin-orbit components (spin-orbit splitting, 18.5 eV) are labeled as v and u, respectively. The v, v‴, v⁗, and u, u‴ and u⁗ components refer to Ce^{4+} final states, while the v_0, v″ and u_0, u″ components refer to Ce^{3+} final states. The well-defined peak u⁗ at the highest binding energy (BE) is peculiar of Ce^{4+} and can be used as a measure of the Ce^{4+}

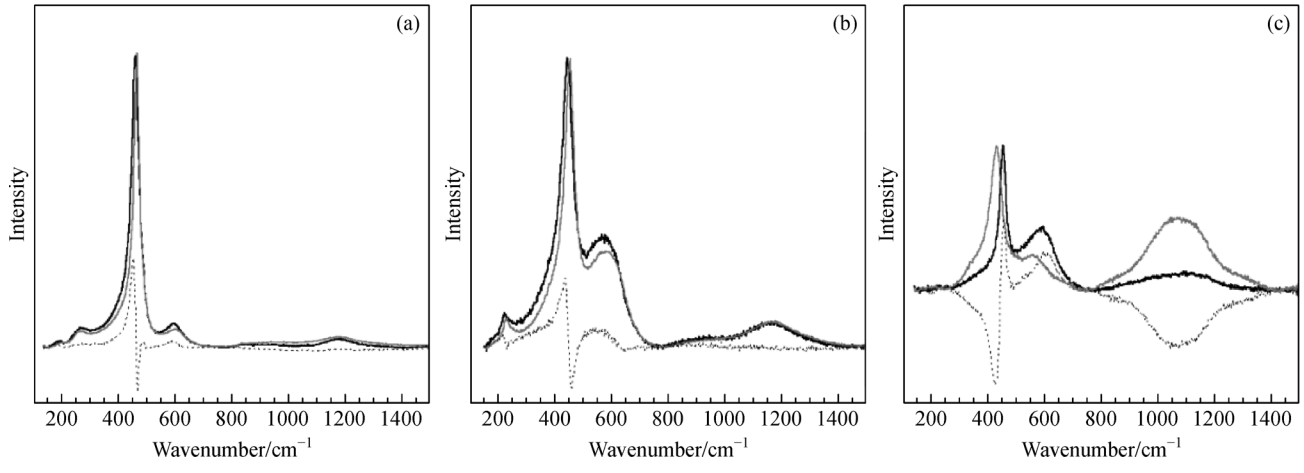

Fig. 3 Raman spectra of (a) CeO_2, (b) 0.3NiCe and (c) 4.0NiCe: before H_2-pretreatment (grey curve); after H_2-pretreatment (black curve); spectral difference between the curves after and before the H_2-pretreatment (dashed curve).

amount [49]. In fully oxidized CeO_2 the area of the u‴″ component should constitute around 14% of the area of the entire Ce3d region [50]. The Ce^{3+} concentration in reduced CeO_2 can instead be more accurately determined by the ratio $Ce^{3+}/(Ce^{3+} + Ce^{4+})$ where the numerator is the sum of the Ce^{3+} signals areas and the denominator is the total area of the Ce3d ($Ce^{3+} + Ce^{4+}$) signals [51–53]. Concerning NiO, the Ni2p region consists of $2p_{3/2}$ and $2p_{1/2}$ spin-orbit components (spin-orbit splitting, 17.2 eV) and associated satellite (separated by 6.1 eV, about 50% of the total intensity), the $2p_{3/2}$ peak being at 854.5 eV [54]. The identification of Ni species in doped systems, originating from defective sites on the surface (Ni^{3+} surface species) or in the bulk due to the formation of a solid solution, has long been debated, leading to the assignment of BE values in the range 855.8–856.4 eV [55,56]. As for oxygen (Fig. S5(b)), the O1s BE for CeO_2 can vary between 529.6 and 530.3 eV, corresponding to Ce^{4+}–O and Ce^{3+}–O bonds, respectively. Surface OH groups are expected to contribute a component at a BE of 531.6 eV [57]. Similar values are reported in the literature for NiO, with O1s peaks at 529.1 and 530.9 eV assigned to the lattice oxygen and to the defective sites on the NiO surface, respectively [55].

The XPS spectra collected on CeO_2 and on the *x*NiCe samples in their oxidized form are illustrated in Fig. 4. The partial superimposition of the $Ce3d_{5/2}$ and $Ni2p_{3/2}$ regions originated complex features which were resolved by curve fitting. It can be noted that the Ni2p components become predominant with increasing Ni content and Ni species as NiO and $Ni(OH)_2$ are detected.

For the *x*NiCe samples, the curve fitting procedure yielded distinct features arising from Ce^{4+} and Ce^{3+} species as well as from Ni^{2+} (NiO, $Ni(OH)_2$) and defective Ni states (Ni^{3+}). Similar trends were obtained for all the samples, indicating that the nature of the specific Ni and Ce surface species do not change significantly with increasing NiO content.

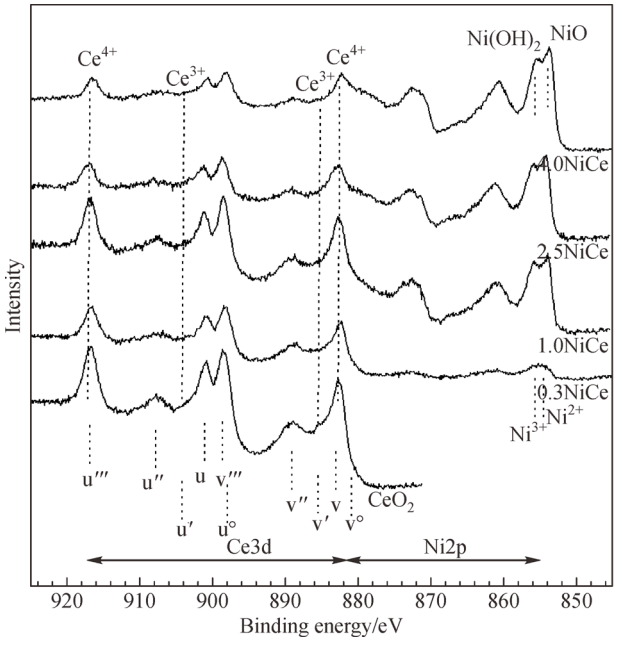

Fig. 4 XPS spectra of CeO_2 and *x*NiCe samples.

Since the 0.3NiCe sample presents the lowest contribution of NiO as a separate phase (as can be inferred from both the corresponding XRD pattern (Fig. S1(a)) and Raman spectrum (Fig. 2)), it was considered as a representative case to investigate the interaction between NiO and CeO_2 oxides. The Ce3d region is resolved with components due to Ce^{4+} (v, v‴, v⁗ and u, u‴, u⁗) and to Ce^{3+} (v″, u″) species (Fig. 5(a)). The amount of Ce^{3+} surface species accounts for 16% of the total intensity, a value higher than that calculated for the pure CeO_2 (11%). This result suggests the existence of Ce^{3+} species other than those due to X-ray irradiation, which reasonably arise from the interaction with Ni species, indicating that the presence of Ni atoms alters the chemical environment of the cerium atoms. The Ni2p region was analyzed for the $Ni2p_{3/2}$ component to overcome the difficulty due to the partial overlap with the Ce3d region and to the complexity of the Ni2p spectroscopic features. The $Ni2p_{3/2}$ signal (Fig. 5(b)) is reproduced with peaks at 854.4, 855.8 and 857.3 eV (and associated satellites), ascribable to Ni^{2+} as NiO, Ni^{3+} species, and Ni^{2+} as Ni $(OH)_2$, respectively. The Ni^{3+} component could correspond to defective sites at the NiO-CeO_2 interface, where Ni species are in strong interaction with the support [55,57], whereas the presence of $Ni(OH)_2$ species is most likely due to exposure of the samples to the atmosphere. The O1s region (Fig. 5(c)) is fitted with a main peak at 529.3 eV, due to lattice oxygen in CeO_2 and NiO, and with two less intense peaks at 530.7 and 532.3 eV, which are assigned to surface oxygen species resulting from the incorporation of Ni^{2+} in the CeO_2 lattice and to surface hydroxyl groups, respectively [55,57]. The peak fitting procedure applied to the 1.0NiCe, 2.5NiCe and 4.0NiCe samples for the Ce3d and $Ni2p_{3/2}$ regions (Figs. S6–S8, cf. ESM)) revealed the same surface species found for 0.3NiCe, i.e., Ce^{4+} and Ce^{3+}; Ni^{2+} (NiO, $Ni(OH)_2$) and Ni^{3+} (resulting from the strong interaction between NiO and CeO_2 outer layers). The same oxygen species (lattice oxygen, surface oxygen due to NiO-CeO_2 interaction, and hydroxyl groups) were also found in all the *x*NiCe samples.

By using the sensitivity factors method, the surface atomic composition was determined by integrating the XPS peaks area of the Ni and Ce species and the results are shown in Table 2 (the calculation details are reported in Tables S1 and S2 (cf. ESM) for CeO_2 and *x*NiCe samples, respectively). The calculated surface Ni/Ce atomic ratios can be compared to those obtained for the bulk by ICP-AES (see Table 1). A Ni surface enrichment is always observed, which is parallel to the increase in the contribution of NiO as a segregate phase with increasing Ni/Ce molar ratios, evidenced by both the XRD and the

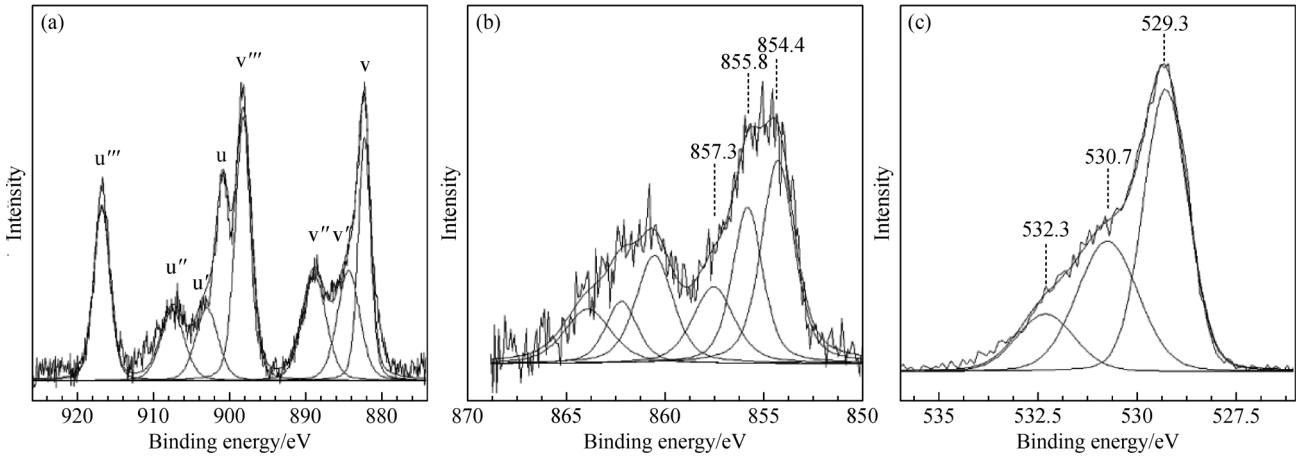

Fig. 5 XPS spectra of the 0.3NiCe sample: (a) Ce3d, (b) Ni2$p_{3/2}$ and (c) O1s regions.

Table 2 Surface composition of the *x*NiCe samples

Sample	$(n_{Ni}/n_{Ce})_{surface}$	$(n_{Ni^{3+}}/n_{Ni,\ total})_{surface}$ [a)]	$(n_{Ce^{3+}}/n_{Ce,\ total})_{surface}$ [b)]
CeO_2	–	–	0.11
0.3NiCe	0.35	0.36	0.18
1.0NiCe	1.60	0.32	0.16
2.5NiCe	3.41	0.31	0.17
4.0NiCe	5.50	0.32	0.17

a) areas ratio of Ni^{3+} (NiO-CeO_2 interacting Ni species) component to the total area of the Ni2$p_{3/2}$ region [Ni^{2+} (NiO, $Ni(OH)_2$) + Ni^{3+}]; b) areas ratio of Ce^{3+} (v″, u″) signals to the total area of the Ce3d region [Ce^{3+} (v″, u″) + Ce^{4+} (v, v‴, v⁗ + u, u‴, u⁗)].

Raman results. Interestingly, the values of the Ni^{3+}/Ni_{total} and Ce^{3+}/Ce_{total} atomic ratios remain almost constant for all the samples in the series (Table 2), indicating that the fraction of Ni species strongly interacting with CeO_2 at surface and/or subsurface level is independent of the Ni content. The increase in the amount of Ce^{3+} surface species with respect to that obtained for pure CeO_2 also suggests that the presence of Ni atoms alters the chemical environment of the cerium atoms, in line with the Raman results.

The microcalorimetric results for the *x*NiCe catalysts after the H_2-pretreatment are reported in Fig. 6 in terms of the differential heat of adsorption as a function of the CO_2 uptake. The Q_{diff} vs. CO_2 uptake curves of the reduced CeO_2 and NiO soft-templated oxides are also reported for comparison. It can be observed that Q_{diff} continuously decreases with the increasing surface coverage, indicating the presence of energetically heterogeneous adsorbing sites. It is worthy of note that the presence of nickel up to a Ni/Ce molar ratio of 2.5 induces an increase in the basic character with respect to CeO_2, all the corresponding microcalorimetric curves lying above that of the pure oxide. Noteworthy, after the marked increase in basicity by addition of the lowest content of nickel, further increasing its amount leads to a concomitant decrease in the basic character, which in the case of 4.0NiCe is even lower than that of the pure cerium oxide, as indicated by the corresponding calorimetric curve located below that of ceria. Nevertheless, it still possesses some basicity, as indicated by the presence of a not negligible number of sites with Q_{diff} greater than 100 kJ·mol^{-1}. For NiO, the surface basic properties are very scarce, as expected by considering that only the residual nickel oxide still present after the H_2-pretreatment is able to adsorb the CO_2 probe molecule. From the Q_{diff} vs. CO_2 uptake curves, it is possible to estimate the strength distribution of the basic sites. A Q_{diff} value of 40 kJ·mol^{-1}, corresponding to about three times the CO_2 condensation heat at 80 °C (13.7 kJ·mol^{-1}), has been considered as the threshold value between chemical and physical or nonspecific adsorption, sites with lower adsorption heats have hence been neglected when assessing basicity. Basic sites have been divided into weak ($40 \leqslant Q_{diff} < 90$ kJ·mol^{-1}), medium ($90 \leqslant Q_{diff} \leqslant 150$ kJ·mol^{-1}), and strong ($Q_{diff} > 150$ kJ·mol^{-1}) sites. The obtained results are summarized in Table 3. The aforementioned trend of the basicity as a function of the Ni content is confirmed by the changes in the site strength distribution: a manifest increase in the basic sites concentration irrespective of their strength is first observed by addition of the lowest amount of nickel to the pure CeO_2; then, a decrease in concentration of the weak- and medium-strength sites, as well as in that of the sites on which CO_2 is irreversibly adsorbed, is observed with increasing Ni content, while the number of strong

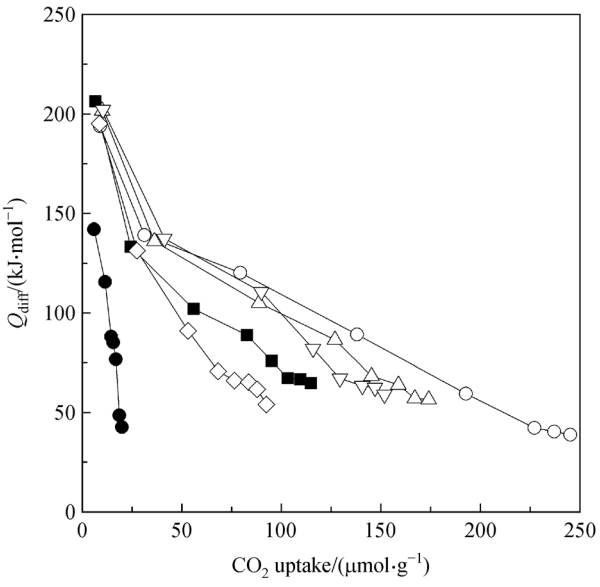

Fig. 6 Differential heat of adsorption as a function of CO_2 uptake for the CeO_2 and NiO pure oxides and *x*NiCe catalysts, after the H_2-pretreatment at 400 °C: (■) CeO_2; (○) 0.3NiCe; (△) 1.0NiCe; (▽) 2.5NiCe; (◇) 4.0NiCe; (●) NiO.

basic sites is much less affected. It has been reported in the literature that the surface basicity of ceria can be enhanced by the presence of oxygen vacancies [58–60] and that the concentration of such vacancies can be tuned by doping CeO_2 with different metal oxides [61,62] owing to the size/charge mismatch between host cerium ions and dopant ions. A manifest increase in the number of oxygen vacancies was observed for Cu- and La-doped CeO_2 prepared by a surfactant-template method [62]. In accordance with the literature, it can be proposed that the presence of Ni, by increasing oxygen vacancies, as confirmed by Raman analysis, enhances the basic character of the NiCe catalysts. However, as the amount of Ni increases, the exposed surface of ceria decreases, which leads to a diminution of both the accessibility and the number of sites responsible for CO_2 adsorption. This may explain the decrease in CO_2 uptake and basic sites strength along with the increase in the Ni content.

Surface basic properties of metal oxides can generally be ascribed to the presence of basic hydroxyl groups (OH) and basic surface oxygens (O^{2-}), which can react directly with CO_2 producing, respectively, hydrogen carbonate and carbonate species. FTIR technique provides a powerful means of investigation of the surface properties of the metal oxides [59,62–64], by studying the interaction with probe molecules. FTIR spectra in the region 2000–1190 cm^{-1}, collected at room temperature on reduced NiO, CeO_2, and selected *x*NiCe samples (0.3NiCe and 2.5NiCe) in contact with CO_2 (CO_2 pressure equal to 5×10^3 Pa), are shown in Fig. 7 (solid lines). The figure also reports spectra obtained after outgassing for 30 min at the same temperature (dashed lines). The FTIR spectra of 2.5NiCe, 0.3NiCe and CeO_2 display broad signals characterized by the presence of distinct bands with different intensities, indicating, in agreement with the microcalorimetric measurements, the presence of a heterogeneous surface, in which sites of different nature and strength exist [63]. After CO_2 adsorption, the 2.5NiCe sample shows a spectrum with at least five partially superimposed contributions. According to the literature [64], the bands centered at about 1614, 1405 and 1214 cm^{-1} can be mainly ascribed to the presence of hydrogen carbonates (HC). However, a contribution of weaker hidden signals due to bidentate and monodentate carbonates (MC, typically observed at about 1580 and 1360 cm^{-1}, respectively) is suggested by the appearance of two shoulders at about 1510 (MC) and 1315 cm^{-1} (bidentate carbonates (BC)), due to the interaction of CO_2 with basic surface O^{2-} species. As expected, a decrease in the intensity of the bands is observed because of the outgassing procedure, though to a lesser extent in the case of the MC, for which a higher stability can be supposed. Similar features appear in the spectra of the 0.3NiCe sample, which exhibit bands very similar to those observed for 2.5NiCe, in terms of both frequencies and relative intensities. Concerning the pure CeO_2 oxide, the most intense peak observed after CO_2 adsorption is centered around 1594 cm^{-1} and this can be reasonably explained by the superimposition of the signals of HC and BC. The presence of HC is also clearly pointed out by the observation of bands at about 1409 and 1216 cm^{-1}, the former characterized by an evident tail towards

Table 3 Microcalorimetric results for the *x*NiCe catalysts and for the pure CeO_2 and NiO oxides after the H_2-pretreatment at 400 °C

Sample	$n_{B,w}$ [a)]/(μmol·g^{-1})	$n_{B,m}$ [b)]/(μmol·g^{-1})	$n_{B,s}$ [c)]/(μmol·g^{-1})	$n_{B,tot}$ [d)]/(μmol·g^{-1})	$n_{B,irr}$ [e)]/(μmol·g^{-1})
CeO_2	35	60	20	115	26
0.3NiCe	101	109	27	237	129
1.0NiCe	55	88	31	174	71
2.5NiCe	43	74	35	152	54
4.0NiCe	39	32	22	93	31
NiO	6	14	–	20	6

a) weak basic sites, $40 \leqslant Q_{diff} < 90$ kJ·mol^{-1}; b) medium basic sites, $90 \leqslant Q_{diff} \leqslant 150$ kJ·mol^{-1}; c) strong acid sites, $Q_{diff} > 150$ kJ·mol^{-1}; d) total basic sites, $Q_{diff} \geq 40$ kJ·mol^{-1}; e) sites on which CO_2 is irreversibly adsorbed at 133 Pa and 80 °C, calculated by the difference in the amount of CO_2 adsorbed between the first and the second adsorption run.

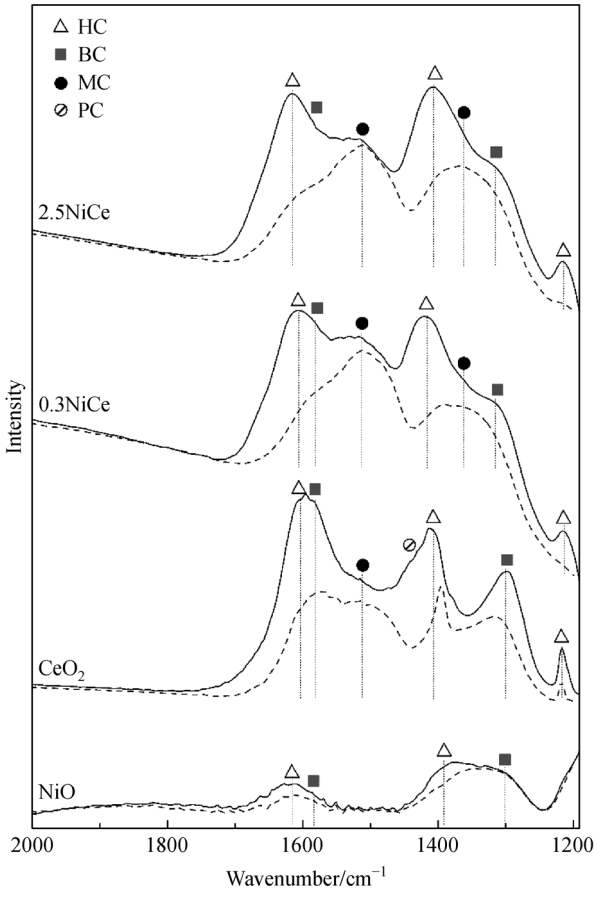

Fig. 7 FTIR spectra of CO_2 adsorbed at room temperature (solid lines; equilibrium pressure: 5×10^3 Pa) and after outgassing (dashed lines; residual pressure: 10^{-1} Pa) for 30 min at the same temperature on reduced NiO, CeO_2, 0.3NiCe and 2.5NiCe samples.

higher frequencies, possibly associated with polydentate carbonates (PC) [64]. In addition, a well-defined peak ascribable to BC can be observed around 1300 cm^{-1}, while the little hump at about 1510 cm^{-1} accounts for the presence of MC. The contribution at about 1510 cm^{-1} becomes slightly more visible after outgassing, confirming the higher stability of the monodentate species with respect to the other carbonate types. In particular, it has been reported in the literature that the formation of monodentate or BC strictly depends on the basicity of the surface oxygen atoms, with stronger sites associated with the formation of monodentate species [63]. A closer inspection of the CeO_2 spectra in comparison with those of 0.3NiCe and 2.5NiCe reveals a different distribution between monodentate and BC. The contributions of the monodentate species become more evident in the presence of Ni, in particular in the spectra recorded after outgassing, suggesting that the presence of Ni gives rise to a higher concentration of stronger sites. It is worthy of note that this observation is in agreement with the microcalorimetric results, from which an increase in the amount of medium- and high-strength basic sites with the increase in nickel content was observed up to a Ni/Ce ratio equal to 2.5. Compared to the other oxides, NiO spectra point out a lower amount of carbonate species (bands with low intensity) and the absence of MC, suggesting a poor basic character, as already revealed by microcalorimetry.

The specific surface areas of the Ni^0 metal particles, expressed per unit mass of either nickel (A_{Ni}) or catalyst (A_{cat}) (Table 4), were determined by means of H_2-TPD analyses performed on the reduced catalysts. It is worth noting that, although H_2 chemisorption and desorption techniques are often used for determining metal surface area on Ni-based materials [65–67], the possible occurrence of spillover phenomena [66,68] in the presence of ceria could cause an overestimation of the A_{Ni} and A_{cat} values. In the light of this, the calculated specific surface areas should be considered as relative data, which anyway allow the evaluation of the capacity of the *x*NiCe catalysts to adsorb H_2 (either on the metal surface or as a consequence of spillover). From the results, a decrease in the A_{Ni} value can be observed with the increase in the Ni/Ce molar ratio, which appears particularly evident passing from 0.3NiCe to 1.0NiCe. Unfortunately, due to the possible simultaneous reduction of both NiO and CeO_2, and by considering that NiO reduction seems to be incomplete (as indicated by XRD in Fig. S1(b) for 2.5NiCe and 4.0NiCe and by HRTEM for 1.0NiCe), the A_{Ni} values cannot be directly related to the dispersion of the Ni^0 metal particles, even more so if a contribution of spillover exists. Nevertheless, the high A_{Ni} value of the 0.3NiCe sample seems to be in agreement with the absence of Ni^0 reflections in its XRD pattern (Fig. S1(b)), which could depend on the high dispersion of the Ni^0 nanocrystals. As expected, the metal surface area per unit mass of catalyst, A_{cat}, increases along with the nickel content up to 2.5NiCe, whereas very similar values are instead observed for the 2.5NiCe and 4.0NiCe samples. Taking into account the comparable Ni^0 crystallites size (*ca.* 8 nm), such similar A_{cat} values could be explained by the presence of a comparable amount of Ni^0 nanoparticles, possibly due to a lower degree of reduction of the original NiO phase on the latter catalyst.

Table 4 Specific Ni^0 metal area expressed per nickel mass unit (A_{Ni}) and catalyst mass unit (A_{cat})

Sample	$A_{Ni}/(m^2\cdot g_{Ni}^{-1})$	$A_{cat}/(m^2\cdot g_{cat}^{-1})$
0.3NiCe	65.7	5.7
1.0NiCe	36.5	8.4
2.5NiCe	25.8	10.6
4.0NiCe	21.8	10.7

3.2 Catalytic results

The results of the catalytic tests carried out on the *x*NiCe catalysts at 300 °C, $CO/CO_2/H_2$ molar ratios equal to

Table 5 Average (6 h) CO (X_{CO}) and CO_2 (X_{CO_2}) conversions and selectivity to methane (S_{CH_4}) of the *x*NiCe catalysts [a)]

Sample	X_{CO}/mol-%	X_{CO_2}/mol-%	S_{CH_4}/mol-%
0.3NiCe	98	57	> 99
1.0NiCe	> 99	74	> 99
2.5NiCe	> 99	81	> 99
4.0NiCe	> 99	80	> 99

a) Reaction conditions: $T = 300$ °C; $P = 1.013 \times 10^5$ Pa; $m_{cat} = 0.050$ g; $CO/CO_2/H_2 = 1/1/7$; $SV = 72000$ $cm^3 \cdot h^{-1} \cdot g_{cat}^{-1}$.

1/1/7, and $SV = 72000$ $cm^3 \cdot h^{-1} \cdot g_{cat}^{-1}$ are summarized in Table 5. Pure ceria was also tested for comparison and it showed to be inactive in the co-methanation reaction. For all the *x*NiCe samples, catalytic activity was found to be stable within 6 h on stream (t.o.s), therefore average values for CO and CO_2 conversions (X_{CO} and X_{CO_2}, respectively) and selectivity to methane (S_{CH_4}) are reported. Irrespective of the catalyst composition, a CH_4 selectivity higher than 99 mol-% is always observed (traces of ethane were detected in some cases), suggesting that the occurrence of reactions leading to the formation of carbon residues can be ruled out. Moreover, all the catalysts exhibit X_{CO} close to 100 mol-%, while X_{CO_2} increases up to *ca.* 80 mol-% by increasing the Ni/Ce molar ratio up to 2.5 and then remains constant. Hydrogenation of CO has already been reported to be favored in comparison with that of CO_2 [30,35,36]. For a $CO/CO_2/H_2$ molar composition of 1/1/7, equilibrium conversions of about 100 and 93 mol-% for CO and CO_2, respectively, were calculated at 300 °C by Gao et al. by means of the total Gibbs free energy minimization method [27]. The present results indicate that, unlike that of CO, which is very close to 100 mol-%, CO_2 conversion does not reach the equilibrium value, suggesting that kinetic factors (possibly related to the different reaction mechanisms by which CO and CO_2 methanation occurs) rather than thermodynamics are responsible for these observations.

In CO hydrogenation, metal Ni^0 species are considered responsible for the activation of CO and H_2, leading to adsorbed carbon (C_{ads}) and hydrogen (H_{ads}) species, which are reported as the intermediates in the production of methane [9,69]. Accordingly, CeO_2 can be considered not directly involved in the previous reaction, although, in its partially reduced form (CeO_{2-x}), it is reported to be beneficial in favoring an easier CO dissociation through its ability to accept oxygen [11,70]. On the other hand, the presence of ceria and, in particular, the occurrence of strong Ni-Ce interactions are reported to be crucial for obtaining high catalytic performances in the hydrogenation of CO_2 to methane, whose main reaction pathway does not involve CO as a reaction intermediate [16,17,71], at variance with the mechanism proposed for Ni/SiO_2 [71] and Ni/Al_2O_3 [72] catalysts. The proposed reaction mechanisms for the CO and CO_2 hydrogenation reactions are depicted in Scheme 2.

Indeed, for the present samples the existence of strongly interacting Ni and Ce species is indicated by the Raman and XPS results (which are also in agreement with previous TPR data [17]). Moreover, as highlighted by the microcalorimetric and FTIR results, CeO_2 is able to effectively adsorb CO_2, forming carbonates and HC, which would be subsequently hydrogenated to formates and finally to methane by hydrogen dissociatively adsorbed on Ni^0 particles. In light of these mechanisms, the catalytic behavior observed along the *x*NiCe series might be elucidated on the basis of the different nature of the sites responsible for activating CO, H_2 and CO_2. Passing from 0.3NiCe to 4.0NiCe, X_{CO} is always very close to the equilibrium value, indicating that, even for the catalyst with the lowest Ni content, the number and the efficacy of the Ni^0 metal sites are such that all the CO molecules supplied can be activated and hydrogenated to methane. By converse, X_{CO_2} progressively rises going from 0.3NiCe to 2.5NiCe, in parallel with the increase in the A_{cat} value (Table 4). Noteworthy, the increase in such parameter, related to the Ni content, is associated with a diminution in the number of basic sites on which CO_2 is

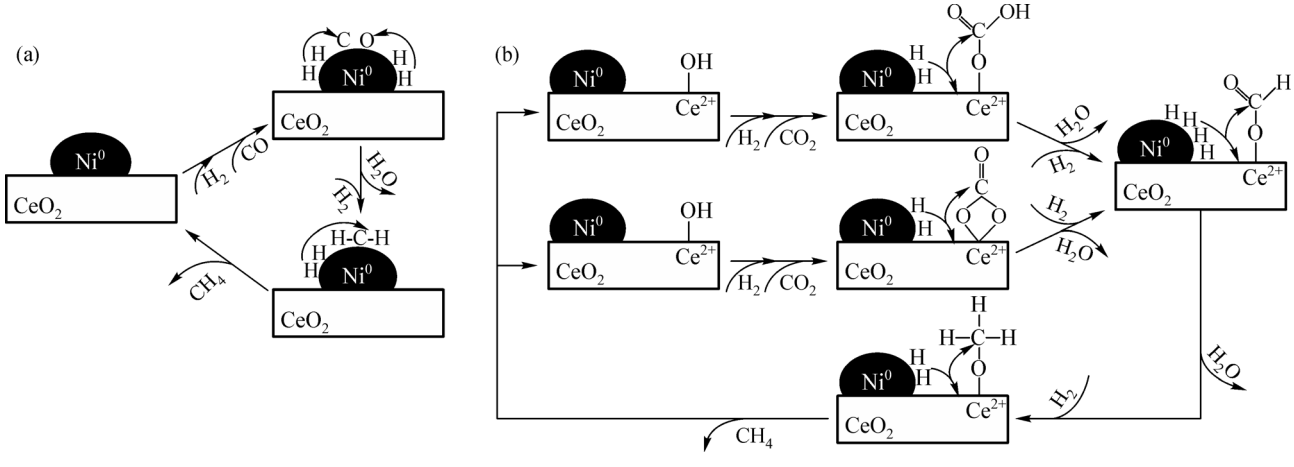

Scheme 2 Proposed mechanisms for (a) the CO and (b) CO_2 hydrogenation to methane.

activated (Table 3), due to the decrease in the amount of ceria. These results hence suggest that the conversion of CO_2 is principally governed by the amount of H_{ads} species available for its hydrogenation, such amount would be limited by the competition between CO and H_2 for the same Ni^0 sites and should reasonably become higher with the increase in the specific metal area. The comparable catalytic activity of 2.5NiCe and 4.0NiCe (Table 5) can therefore be explained by their very similar A_{cat} values (Table 4).

It could be hypothesized that the preferential conversion of carbon monoxide is related to its quicker hydrogenation when compared to CO_2, due to the proximity of the sites on which both CO and H_2 are activated, which would favor the reaction between the C_{ads} and H_{ads} intermediates rather than migration of the H_{ads} species by spillover processes toward the ceria sites on which HC and carbonates (coming from CO_2 activation) can be hydrogenated. However, in addition to methanation (Scheme 1), CO and CO_2 could also be involved in the reverse methane dry reforming and in the water gas shift reactions (Scheme 3). Indeed, both reactions are thermodynamically favored at 300 °C (the equilibrium constant for the reaction of reverse methane dry reforming is even higher than those of the methanation reactions) [27,73]. Moreover, NiCe-based systems have been reported as active catalysts for the water gas shift [74,75] and the methane dry reforming reactions [76,77]. Notably, reverse dry reforming has been reported to be the main reaction for CO hydrogenation at low H_2/CO molar ratios with La_2O_3-promoted Ni/Al_2O_3 [73] and Ni/SiO_2 [78] at temperatures between 300 °C and 550 °C. Consequently, it might be possible that not only the hydrogenation of CO_2 is repressed by the competitive CO methanation, but also that the occurrence of the reverse dry methane reforming and/or the water gas shift reactions, through which carbon dioxide is formed, can lead to an overall lower conversion of CO_2.

$$2CO + 2H_2 \leftrightarrows CH_4 + CO_2 \quad \Delta H = -247.3\ kJ\cdot mol^{-1} \quad (1)$$

$$CO + H_2O \leftrightarrows CO_2 + H_2 \quad \Delta H = -41.2\ kJ\cdot mol^{-1} \quad (2)$$

Scheme 3 Stoichiometric equations for: (1) reverse methane dry reforming and (2) water gas shift.

At a much higher space velocity (450000 $cm^3\cdot h^{-1}\cdot g_{cat}^{-1}$), the 1.0NiCe, 2.5NiCe and 4.0NiCe catalysts are stable within the investigated 6 h on stream (Fig. 8), with methane as the only product. Though decreasing slightly with the increase in SV, X_{CO} remains very high (96–98 mol-%) and close to the equilibrium value regardless of the Ni content, indicating that a significant portion of Ni^0 sites still remains active in these severe reaction conditions. A pronounced effect of the increase in space velocity is instead observed on CO_2 conversion, which decreases by about 20 mol-% for the three samples. Interestingly, 2.5NiCe and 4.0NiCe show the same catalytic behavior also in these conditions, confirming what previously observed at the lower SV value (72000 $cm^3\cdot h^{-1}\cdot g_{cat}^{-1}$).

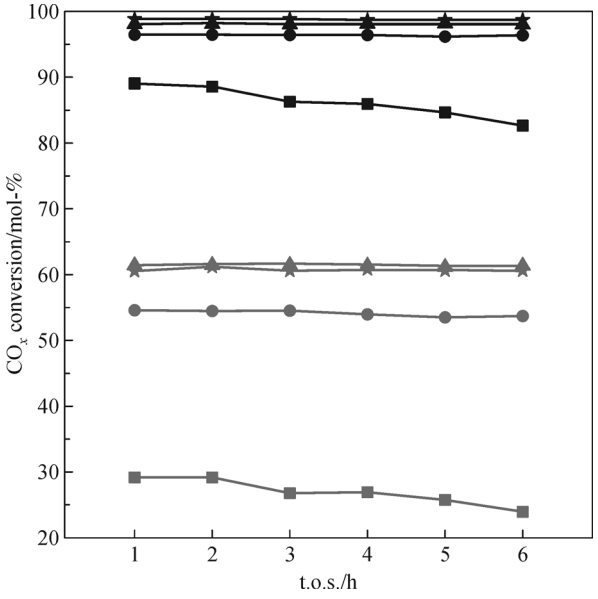

Fig. 8 CO (black symbols) and CO_2 (grey symbols) conversions for 0.3NiCe (■,■), 1.0NiCe (●, ●), 2.5NiCe (▲,▲), and 4.0NiCe (✶, ✶). Reaction conditions: $P = 1.013\times10^5$ Pa; T = 300°C; CO/CO_2/H_2 molar ratio equal to 1/1/7; SV = 450000 $cm^3\cdot g_{cat}^{-1}\cdot h^{-1}$.

These results highlight that the increase in space velocity further disadvantages the hydrogenation of CO_2 with respect to that of CO. Compared to the other catalysts in the series, the catalytic behavior of 0.3NiCe appears significantly different (Fig. 8), besides showing a manifest decrease (which is much more pronounced for CO_2, whose conversion decreases by about 47% compared to that at the lower space velocity), CO and CO_2 conversion values also decline with time-on-stream. Considering that S_{CH_4} was around 88 mol-%, with only traces of ethane detected as a byproduct, the evident deactivation of this catalyst can supposedly be associated with the formation of carbonaceous deposits on its surface, which, interestingly, appears to be promoted by the low contact time. Carbon analysis, performed on fresh and post-reaction 0.3NiCe and 1.0NiCe catalysts, confirms this hypothesis. While only a slight increase in the percentage of carbon is observed in the 1.0NiCe catalyst after the reaction (values of 0.2 and 1.0 wt-% are obtained for the fresh and post-reaction samples, respectively), a significant formation of carbonaceous species results for 0.3NiCe after the reaction, whose carbon content passes from 0.1 (fresh) to 4.8 wt-% (post-reaction). It is worth noting that such a difference between 0.3NiCe and 1.0NiCe appears even more significant if the carbon content on the post-reaction samples is expressed per unit mass of nickel, i.e., the catalytic active species on which carbonaceous deposits

can mainly be supposed to form. The obtained results, 4.1 and 55.4 wt-% for 1.0NiCe and 0.3NiCe, respectively, clearly show the much greater tendency of the 0.3NiCe catalyst to deactivate. To get information on the nature of the carbonaceous species, a TGA was performed, and the results are shown in Fig. S9 (cf. ESM). Weight losses of about 1.3% and 5.0% have been obtained at high temperature (~640 °C) for 1.0NiCe and 0.3NiCe, respectively (Fig. S9(a)). Such losses, well evidenced in the DTG curve (Fig. S9(b)) correspond to an exothermic process (Fig. S9(c)), which can reasonably be ascribed to the combustion of carbon-like species [79], suggesting the occurrence of CO disproportionation.

It was reported in the literature that on NiCe-based catalysts the establishment of strong interactions between C_{ads} species and Ni^0 metal sites, which are favored in the presence of small Ni^0 particles, can lead to the deactivation of the catalyst due to the possible occurrence of the Boudouard reaction (Scheme 4), through which carbon is formed [9].

$$2CO \leftrightarrows C + CO_2 \quad \Delta H = -172.5\ kJ \cdot mol^{-1}$$

Scheme 4 Stoichiometric equation for the CO disproportionation (Boudouard) reaction.

Considering that very small Ni^0 particles are supposed to form on the 0.3NiCe sample, its deactivation can be explained accordingly: due to the low nickel content, the amount of hydrogen activated at high *SV* on this catalyst would be insufficient to reduce a significant portion of the C_{ads} species formed, which therefore tend to polymerize forming carbon deposits. Taking into account the small Ni^0 crystallites size ($\leqslant$8 nm), a preferential adsorption and activation of CO with respect to H_2 might also be hypothesized for the other *x*NiCe catalysts, which could explain the notable decrease in CO_2 conversion at high space velocity (Fig. 8); unlike the case of 0.3NiCe, due to the higher Ni content, the available amount of H_{ads} is however sufficient to hydrogenate CO almost completely. In order to verify the role of carbon monoxide in the deactivation of the catalyst, CO methanation tests were carried out on 0.3NiCe and 1.0NiCe at the same temperature and *SV*, using a H_2/CO molar ratio equal to 3 (stoichiometric). At 72000 $cm^3 \cdot h^{-1} \cdot g_{cat}^{-1}$, no deactivation phenomena were observed after 24 h of reaction, with CO conversions of 98 and 100 mol-% for 0.3NiCe and 1.0NiCe, respectively. Besides methane, a significant amount of carbon dioxide was detected (S_{CO_2} equal to 16 and 11 mol-% for 0.3NiCe and 1.0NiCe, respectively), possibly formed through the reverse methane dry reforming and/or the water gas shift reactions (Scheme 3). A very different catalytic behavior was instead observed at 450000 $cm^3 \cdot h^{-1} \cdot g_{cat}^{-1}$, while 1.0NiCe still exhibited a constant catalytic performance within 24 h on stream (X_{CO} = 84 mol-%, S_{CH_4} = 84 mol-%, S_{CO_2} = 16 mol-%), 0.3NiCe was completely deactivated after 1 h of reaction. This result is not surprising and clearly confirms the involvement of carbon monoxide in the deactivation of 0.3NiCe at high *SV*. Proof of the possible occurrence of the Boudouard reaction was also obtained by performing CO-TPD analyses on the same samples. In the TPD profiles (Fig. S10, cf. ESM), collected by a massspectrometer detector, a clear contribution of CO does not appear, while a noticeable signal ascribable to CO_2 is observed in the range 150 °C–500 °C for both catalysts. These findings highlight the ability of the catalysts to promote CO disproportionation that, as revealed by the catalytic results, can become significant even in the presence of hydrogen when the number of Ni^0 sites and the reaction conditions adopted are not suitable to ensure the activation of a proper amount of H_2.

With the aim of evaluating the performance of the catalysts using a feed composition similar to that of a generic syngas (for which H_2 is usually in defect with respect to the stoichiometric amount imposed by the CO and CO_2 methanation reactions (Scheme 1)), further co-methanation tests were carried out at 300 °C, with a CO/CO_2/H_2 molar composition equal to 1/1/5, and a space velocity of 72000 $cm^3 \cdot h^{-1} \cdot g_{cat}^{-1}$. The relevant results are reported in Table 6. The catalysts were stable during the 6-hour tests, with a CH_4 selectivity higher than 99 mol-%. Despite the less favorable H_2/CO_x molar ratio, X_{CO} still results close to 100 mol-%, with a very slight increase passing from 0.3NiCe to 1.0NiCe. On the other hand, X_{CO_2} appears clearly limited by the low concentration of H_2 in the reactant mixture, confirming that the activated hydrogen is preferentially consumed in the conversion of CO. As expected, X_{CO_2} increases with the nickel content up to a Ni/Ce molar ratio equal to 2.5, while, once again, the 2.5NiCe and 4.0NiCe samples are characterized by the same conversion values.

Table 6 Average (6 h) CO (X_{CO}) and CO_2 (X_{CO_2}) conversions and selectivity to methane (S_{CH_4}) of the *x*NiCe catalysts [a)]

Sample	X_{CO}/mol-%	X_{CO_2}/mol-%	S_{CH_4}/mol-%
0.3NiCe	97	29	> 99
1.0NiCe	99	34	> 99
2.5NiCe	99	37	> 99
4.0NiCe	99	38	> 99

a) Reaction conditions: T = 300 °C; $P = 1.013 \times 10^5$ Pa; m_{cat} = 0.050 g; CO/CO_2/H_2 = 1/1/5; *SV* = 72000 $cm^3 \cdot h^{-1} \cdot g_{cat}^{-1}$.

Being the catalyst on which, in the operating conditions discussed so far, the most significant effects on CO_2 conversion were found, without however observing any deactivation phenomena, 1.0NiCe was chosen to perform additional catalytic tests, through which co-methanation was studied in terms of thermal stability and activity at different reaction temperatures and a wide range of *SV*.

Noteworthy, methane was always detected as the only product, confirming the high selectivity of the present catalysts toward hydrogenation in different reaction regimes, provided that the nickel content is appropriate. The conversion values as a function of the reaction temperature in the range 200 °C–500 °C are plotted in Fig. 9(a). From 200 °C to 300 °C, X_{CO} and X_{CO_2} rise with temperature and then diminish because of the exothermicity of both the CO and CO_2 methanation reactions. Thermal stability was studied by carrying out a long-run test (50 h) in which different temperature ranges were investigated up to 500 °C, considering 300 °C as the control value. The results, summarized in Fig. 9(b), highlight that, even after exposure to the temperature of 500 °C, the catalytic activity at 300 °C is always restored, indicating excellent thermal stability of the catalyst.

Finally, the influence of space velocity was studied in the range 48000–450000 $cm^3 \cdot h^{-1} \cdot g_{cat}^{-1}$ (Fig. 10). With the increase in *SV*, X_{CO} and X_{CO_2} decrease by 5% and 29%, respectively, which is coherent with the influence of the contact time on H_2 activation and with the preferential hydrogenation of carbon monoxide. Compared to that of CO, a steeper decrease in the conversion of CO_2 during the co-methanation reaction has already been reported in the literature. For a $Ni/Ce_{0.50}Zr_{0.50}O_2$ catalyst with a nickel content similar to that of the present 1.0NiCe, CO and CO_2 conversions were found to diminish by 5% and 36%, respectively, in the *SV* range between 72000 and 450000 $cm^3 \cdot h^{-1} \cdot g_{cat}^{-1}$, using a substoichiometric amount of H_2 [36]. A decrease in CO_2 conversion of about 23% was instead reported for a Mn-promoted Ni/Al_2O_3 catalyst [33] in a much narrower *SV* range (from 48000 to 84000 $cm^3 \cdot h^{-1} \cdot g_{cat}^{-1}$) while CO conversion remained constant.

4 Conclusions

$NiO\text{-}CeO_2$ mixed oxides, prepared by the soft template method with different Ni/Ce molar ratios (0.3–4.0), were used as catalysts in the CO and CO_2 co-methanation reaction after reduction in H_2 at mild conditions (400 °C for 1 h). At 72000 $cm^3 \cdot h^{-1} \cdot g_{cat}^{-1}$, 300 °C, and $CO/CO_2/H_2$ molar composition equal to 1/1/7, a CH_4 selectivity higher than 99 mol-% was observed, irrespective of the catalyst composition. Whereas CO was almost completely transformed ($X_{CO} \geq 98$ mol-%) on all the *x*NiCe catalysts, the conversion of CO_2 was at most 80 mol-%, considerably lower than the equilibrium value of 93 mol-%, suggesting that kinetic factors rather than thermodynamics play a role. The trend of CO_2 conversion as a function of the Ni/Ce molar ratio suggested that, though the presence of ceria is important for activating CO_2, its hydrogenation is mainly governed by the availability of H_{ads} species, which depends on the metal surface area (A_{cat}). In the presence of a lower H_2 content in the feed ($CO/CO_2/H_2$ = 1/1/5), CO hydrogenation was even more favored with respect to that of CO_2. The explanation proposed for the faster and definitely preferred CO hydrogenation is that, due to the proximity of the sites on which both CO and H_2 are dissociatively adsorbed and activated, the reaction between the C_{ads} and H_{ads} intermediates is favored in comparison with migration of H_{ads} species by spillover processes from the Ni^0 metal sites toward the nearby ceria sites on which CO_2 is activated. The catalytic results obtained at higher *SV* (450000 $cm^3 \cdot h^{-1} \cdot g_{cat}^{-1}$) further supported this hypothesis, highlighting that the hydrogenation of CO_2 is considerably disadvantaged by the increase in space velocity while that of CO is only slightly affected. Moreover, in addition to the competitive CO methanation,

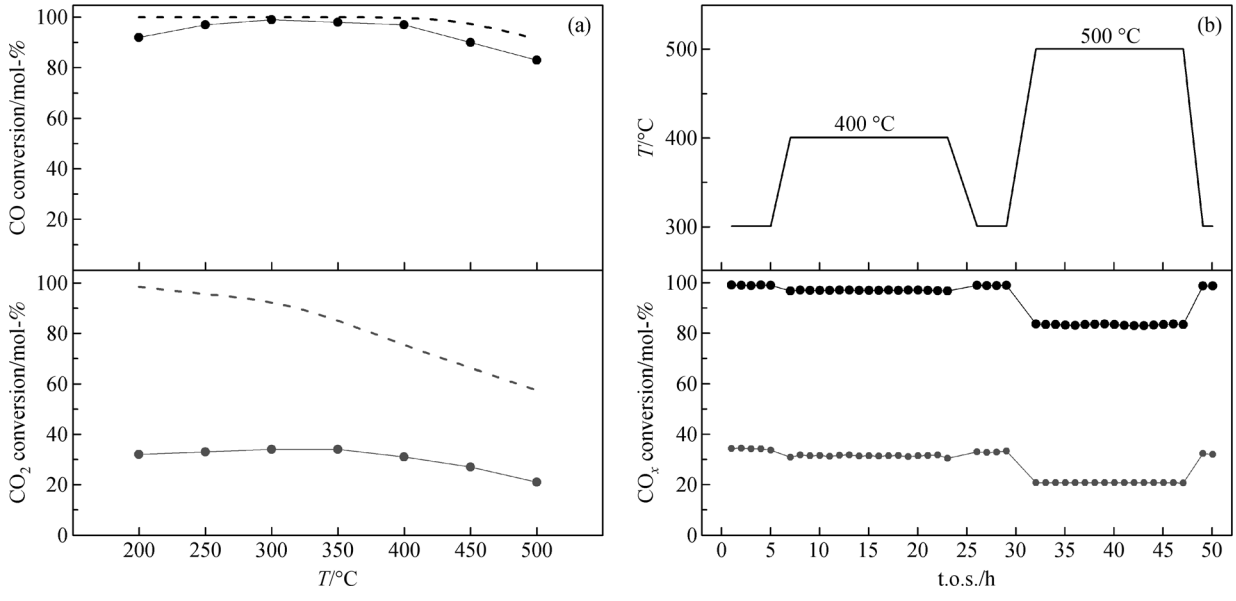

Fig. 9 CO and CO_2 co-methanation results for the 1.0NiCe sample. CO_x conversions as a function of (a) reaction temperature and of (b) t.o.s. by varying the temperature during the run: (●), CO conversion; (●), CO_2 conversion; (- - -), equilibrium conversions. Other reaction conditions: $CO/CO_2/H_2$ = 1/1/5; *SV* = 72000 $cm^3 \cdot h^{-1} \cdot g_{cat}^{-1}$.

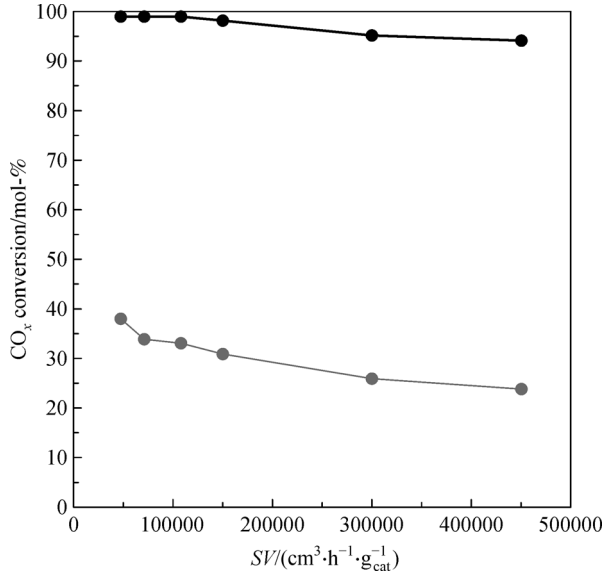

Fig. 10 CO (black curve) and CO_2 (grey curve) conversions as a function of space velocity.

the overall conversion of CO_2 might also be lowered by the occurrence of the reverse dry methane reforming and/or the water gas shift reactions. In the case of the 0.3NiCe catalyst, a manifest decrease in both CO and CO_2 conversions as a function of t.o.s was observed using a stoichiometric amount of H_2 at high space velocity. This deactivation was proven to be caused by deposition of carbon, deriving from the Boudouard reaction, on the Ni^0 metal sites. Such result highlighted the importance of optimizing the Ni content to prevent deactivation and to obtain good catalytic performances for the CO_x co-methanation reaction in a wide range of operating conditions. Indeed, when the number of Ni^0 sites was enough to favor the hydrogenation of CO over its disproportionation, the NiCe investigated system was very promising, being highly active and stable (up to 50 h) also when submitted to thermal stress.

Acknowledgements The authors acknowledge the Department of Science and Technology, Polytechnic of Turin, Italy, for XPS measurements, the University Service Center for Research (CeSAR), University of Cagliari, Italy, for the use of the JEOL JEM 2010 facility, and the "Microanalysis Service", Department of Chemistry, University of Rome "La Sapienza", Italy, for Elemental Analyses.

Electronic Supplementary Material Supplementary material is available in the online version of this article at https://doi.org/10.1007/s11705-020-1951-8 and is accessible for authorized users.

Funding Information Open Access funding provided by Università degli Studi di Cagliari.

References

1. IPCC 2013: Summary for policymakers. In: Stocker T F, Qin D, Plattner G K, Tignor M, Allen S K, Boschung J, Nauels A, Xia Y, Bex V, Midgley P M, eds. Climate Change 2013: the Physical Science Basis. Contribution of Working Group I to the Fifth Assessment Report of the Intergovernmental Panel on Climate Change. Cambridge, UK and New York, USA: Cambridge University Press, 2013
2. Aresta M, Dibenedetto A, Angelini A. The use of solar energy can enhance the conversion of carbon dioxide into energy-rich products: stepping towards artificial photosynthesis. Philosophy Transactions of the Royal Society A, 2013, 371(1996): 20120111
3. CO_2 Emission from Fuel Combustion Highlights. 2016 ed. Paris: International Energy Agency (IEA) Publications, 2016
4. Aresta M, Dibenedetto A, Angelini A. Catalysis for the valorization of exhaust carbon: from CO_2 to chemicals, materials, and fuels. Technological use of CO_2. Chemical Reviews, 2014, 114(3): 1709–1742
5. Wolde-Rufael Y, Idowu S. Income distribution and CO_2 emission: a comparative analysis for China and India. Renewable & Sustainable Energy Reviews, 2017, 74: 1336–1345
6. Gao J, Liu Q, Gu F, Liu B, Zhong Z, Su F. Recent advances in methanation catalysts for the production of synthetic natural gas. RSC Advances, 2015, 5(29): 22759–22776
7. Wang H, Pei Y, Qiao M, Zong B. Advances in methanation catalysis. Catalysis, 2017, 29: 1–28
8. Aziz M A A, Jalil A A, Triwahyono S, Ahmada A. CO_2 methanation over heterogeneous catalysts: recent progress and future prospects. Green Chemistry, 2015, 17(5): 2647–2663
9. Senanayake S D, Evans J, Agnoli S, Barrio L, Chen T L, Hrbek J, Rodriguez J A. Water-gas shift and CO methanation reactions over Ni-CeO_2(111) catalysts. Topics in Catalysis, 2011, 54(1-4): 34–41
10. Carrasco J, Barrio L, Liu P, Rodriguez J A, Ganduglia-Pirovano M V. Theoretical studies of the adsorption of CO and C on Ni(111) and Ni/CeO_2(111): evidence of a strong metal-support interaction. Journal of Physical Chemistry C, 2013, 117(16): 8241–8250
11. Rombi E, Cutrufello M G, Atzori L, Monaci R, Ardu A, Gazzoli D, Deiana P, Ferino I. CO methanation on Ni-Ce mixed oxides prepared by hard template method. Applied Catalysis A, General, 2016, 515: 144–153
12. Liu Y, Zhu L, Wang X, Yin S, Leng F, Zhang F, Lin H, Wang S. Catalytic methanation of syngas over Ni-based catalysts with different supports. Chinese Journal of Chemical Engineering, 2017, 25(5): 602–608
13. Le T A, Kim T W, Lee S H, Park E D. Effects of Na content in Na/Ni/SiO_2 and Na/Ni/CeO_2 catalysts for CO and CO_2 methanation. Catalysis Today, 2018, 303: 159–167
14. Tada S, Shimizu T, Kameyama H, Haneda T, Kikuchi R. Ni/CeO_2

catalysts with high CO_2 methanation activity and high CH_4 selectivity at low temperatures. International Journal of Hydrogen Energy, 2012, 37(7): 5527–5531

15. Zhou G, Liu H, Cui K, Jia A, Hu G, Jiao Z, Liu Y, Zhang X. Role of surface Ni and Ce species of Ni/CeO_2 catalyst in CO_2 methanation. Applied Surface Science, 2016, 383: 248–252
16. Atzori L, Cutrufello M G, Meloni D, Monaci R, Cannas C, Gazzoli D, Sini M F, Deiana P, Rombi E. CO_2 methanation on hard-templated $NiO\text{-}CeO_2$ mixed oxides. International Journal of Hydrogen Energy, 2017, 42(32): 20689–20702
17. Atzori L, Cutrufello M G, Meloni D, Cannas C, Gazzoli D, Monaci R, Sini M F, Rombi E. Highly active $NiO\text{-}CeO_2$ catalysts for synthetic natural gas production by CO_2 methanation. Catalysis Today, 2018, 299: 183–192
18. Ratchahat S, Sudoh M, Suzuki Y, Kawasaki W, Watanabe R, Fukuhara C. Development of a powerful CO_2 methanation process using a structured Ni/CeO_2 catalyst. Journal of CO_2 Utilization, 2018, 24: 210–219
19. Malwadkar S, Bera P, Hegde M S, Satyanarayana C V V. Preferential oxidation of CO on Ni/CeO_2 catalysts in the presence of excess H_2 and CO_2. Reaction Kinetics, Mechanisms and Catalysis, 2012, 107(2): 405–419
20. Zyryanova T, Snytnikov P V, Gulyaev R V, Amosov Y, Boronin A I, Sobyanin V A. Performance of Ni/CeO_2 catalysts for selective CO methanation in hydrogen-rich gas. Chemical Engineering Journal, 2014, 238: 189–197
21. Nematollahi B, Rezaei M, Nemati Lay E. Preparation of highly active and stable $NiO\text{-}CeO_2$ nanocatalysts for CO selective methanation. International Journal of Hydrogen Energy, 2015, 40(27): 8539–8547
22. Nematollahi B, Rezaei M, Nemati Lay E. Selective methanation of carbon monoxide in hydrogen rich stream over Ni/CeO_2 nanocatalysts. Journal of Rare Earths, 2015, 33(6): 619–628
23. Konishcheva M V, Potemkin D I, Snytnikov P V, Zyryanova M M, Pakharukova V P, Simonov P A, Sobyanin V A. Selective CO methanation in H_2-rich stream over Ni-, Co- and Fe/CeO_2: effect of metal and precursor nature. International Journal of Hydrogen Energy, 2015, 40(40): 14058–14063
24. Konishcheva M V, Potemkin D I, Badmaev S D, Paukshtis P V, Sobyanin V A, Parmon V N. On the mechanism of CO and CO_2 methanation over Ni/CeO_2 catalysts. Topics in Catalysis, 2016, 59(15-16): 1424–1430
25. Habazaki H, Yamasaki M, Zhang B P, Kawashima A, Kohno S, Takai T, Hashimoto K. Co-methanation of carbon monoxide and carbon dioxide on supported nickel and cobalt catalysts prepared from amorphous alloys. Applied Catalysis A, General, 1998, 172(1): 131–140
26. Gogate M R, Davis R J. Comparative study of CO and CO_2 hydrogenation over supported RhFe catalysts. Catalysis Communications, 2010, 11(10): 901–906
27. Gao J, Wang Y, Ping Y, Hu D, Xu G, Gu F, Su F. A thermodynamic analysis of methanation reactions of carbon oxides for the production of synthetic natural gas. RSC Advances, 2012, 2(6): 2358–2368
28. Huang Y H, Wang J J, Liu Z M, Lin G D, Zhang H B. Highly efficient $Ni\text{-}ZrO_2$ catalyst doped with Yb_2O_3 for co-methanation of CO and CO_2. Applied Catalysis A, General, 2013, 466: 300–306
29. Razzaq R, Zhu H, Jiang L, Muhammad U, Li C, Zhang S. Catalytic methanation of CO and CO_2 in coke oven gas over $Ni\text{-}Co/ZrO_2\text{-}CeO_2$. Industrial & Engineering Chemistry Research, 2013, 52(6): 2247–2256
30. Razzaq R, Li C, Amin N, Zhang S, Suzuki K. Co-methanation of carbon oxides over nickelbased $Ce_xZr_{1-x}O_2$ catalysts. Energy & Fuels, 2013, 27(11): 6955–6961
31. Razzaq R, Li C, Usman M, Suzuki K, Zhang S. A highly active and stable $Co_4N/\gamma Al_2O_3$ catalyst for CO and CO_2 methanation to produce synthetic natural gas. Chemical Engineering Journal, 2015, 262: 1090–1098
32. Li Y, Zhang Q, Chai R, Zhao G, Liu Y, Lu Y. Structured $Ni\text{-}CeO_2\text{-}Al_2O_3$/Ni-foam catalyst with enhanced heat transfer for substitute natural gas production by syngas methanation. ChemCatChem, 2015, 7(9): 1427–1431
33. Zhao K, Li Z, Bian L. CO_2 methanation and co-methanation of CO and CO_2 over Mn-promoted Ni/Al_2O_3 catalysts. Frontiers of Chemical Science and Engineering, 2016, 10(2): 273–280
34. Belimov M, Metzger D, Pfeifer P. On the temperature control in a microstructured packed bed reactor for methanation of CO/CO_2 mixtures. AIChE Journal. American Institute of Chemical Engineers, 2017, 63(1): 120–129
35. Frontera P, Macario A, Malara A, Modafferi V, Mascolo M C, Candamano S, Crea F, Antonucci P. CO_2 and CO hydrogenation over Ni-supported materials. Functional Materials Letters (Singapore), 2018, 11(05): 1850061
36. Atzori L, Rombi E, Meloni D, Sini M F, Monaci R, Cutrufello M G. CO and CO_2 Co-Methanation on $Ni/CeO_2\text{-}ZrO_2$ Soft-Templated Catalysts. Catalysts, 2019, 9(5): 415
37. Wang Y, Ma J, Luo M, Fang P, He M. Preparation of high-surface area nano-CeO_2 by template-assisted precipitation method. Journal of Rare Earths, 2007, 25(1): 58–62
38. Luo M F, Ma J M, Lu J Q, Song Y P, Wang Y J. High-surface area $CuO\text{-}CeO_2$ catalysts prepared by a surfactant-templated method for low-temperature CO oxidation. Journal of Catalysis, 2007, 246(1): 52–59
39. Wagner C D, Davis L E, Zeller M V, Taylor J A, Raymond R H, Gale L H. Empirical atomic sensitivity factors for quantitative analysis by electron spectroscopy for chemical analysis. Surface and Interface Analysis, 1981, 3(5): 211–225
40. Klug H P, Alexander L E. X-ray diffraction procedures: for polycrystalline and amorphous materials. 2nd ed. New York: John Wiley & Sons Inc., 1974, 687–703
41. Rouquerol F, Rouquerol J, Sing K S W, Llewellyn P, Maurin G. Adsorption by powders and porous solids: principles, methodology and applications. Amsterdam: Academic Press, 2014, 12–13
42. Weber W H, Bass K C, McBride J R. Raman study of CeO_2: second-order scattering, lattice dynamics, and particle-size effects. Physical Review. B, 1993, 48(1): 178–185
43. Spanier J E, Robinson R D, Zheng F, Chan S W, Herman I P. Size-dependent properties of CeO_{2-y} nanoparticles as studied by Raman scattering. Physical Review. B, 2001, 64(24): 245407–245414

44. Taniguchi T, Watanabe T, Sugiyama N, Subramani A K, Wagata H, Matsushita N, Yoshimura M. Identifying defects in ceria-based nanocrystals by UV resonance Raman spectroscopy. Journal of Physical Chemistry C, 2009, 113(46): 19789–19793
45. Mironova-Ulmane N, Kuzmin A, Steins I, Grabis J, Sildos I, Pärs M. Raman scattering in nanosized nickel oxide NiO. Journal of Physics: Conference Series, 2007, 93: 012039–012043
46. Wu Z, Li M, Howe J, Meyer H M III, Overbury S H. Probing defect sites on CeO_2 nanocrystals with well-defined surface planes by Raman spectroscopy and O_2 adsorption. Langmuir, 2010, 26(21): 16595–16606
47. Gao Y, Li R, Chen S, Luo L, Cao T, Huang W. Morphology-dependent interplay of reduction behaviors, oxygen vacancies and hydroxyl reactivity of CeO_2 nanocrystals. Physical Chemistry Chemical Physics, 2015, 17(47): 31862–31871
48. Burroughs P, Hamnett A, Orchard A F, Thornton G. Satellite structure in the X-ray photoelectron spectra of some binary and mixed oxides of lanthanum and cerium. Journal of the Chemical Society, Dalton Transactions: Inorganic Chemistry, 1976, 17(17): 1686–1698
49. Romeo M, Bak K, El Fallah J, Le Normand F, Hilaire L. XPS study of the reduction of cerium dioxide. Surface and Interface Analysis, 1993, 20(6): 5008–5012
50. Shyu J Z, Otto K, Watkins W L H, Graham G W, Belitz R K, Gandhi H S. Characterization of Pd/γ-alumina catalysts containing ceria. Journal of Catalysis, 1988, 114(1): 23–33
51. Zhang F, Wang P, Koberstein J, Khalid S, Chan S W. Cerium oxidation state in ceria nanoparticles studied with X-ray photoelectron spectroscopy and absorption near edge spectroscopy. Surface Science, 2004, 563(1-3): 74–82
52. Qiu L, Liu F, Zhao L, Ma Y, Yao J. Comparative XPS study of surface reduction for nanocrystalline and microcrystalline ceria powder. Applied Surface Science, 2006, 252(14): 4931–4935
53. Allahgholi A, Flege J I, Thieß S, Drube W, Falta J. Oxidation-state analysis of ceria by X-ray photoelectron spectroscopy. ChemPhysChem, 2015, 16(5): 1083–1091
54. Grosvenor A P, Biesinger M C, Smart R S C, McIntyre N S. New interpretations of XPS spectra of nickel metal and oxides. Surface Science, 2006, 600(9): 1771–1779
55. Atanasov M, Reinen D. Non-local electronic effects in core-level photoemission, UV and optical electronic absorption spectra of nickel oxides. Journal of Electron Spectroscopy and Related Phenomena, 1997, 86(1-3): 185–199
56. Carley A F, Jackson S D, O'Shea J N, Roberts M W. The formation and characterisation of Ni^{3+}—An X-ray photoelectron spectroscopic investigation of potassium-doped Ni(110)-O. Surface Science, 1999, 440(3): L868–L874
57. Mahammadunnisa S, Manoj Kumar Reddy P, Lingaiah N, Subrahmanyam C. NiO/$Ce_{1-x}Ni_xO_2$−δ as an alternative to noble metal catalysts for CO oxidation. Catalysis Science & Technology, 2013, 3: 730–736
58. Metiu H, Chrétien S, Hu Z, Li B, Sun X Y. Chemistry of Lewis acid-base pairs on oxide surfaces. Journal of Physical Chemistry C, 2012, 116(19): 10439–10450
59. Wu Z, Mann A K P, Li M, Overbury S H. Spectroscopic investigation of surface-dependent acid-base property of ceria nanoshapes. Journal of Physical Chemistry C, 2015, 119(13): 7340–7350
60. Tumuluri U, Rother G, Wu Z. Fundamental understanding of the interaction of acid gases with CeO_2: from surface science to practical catalysis. Industrial & Engineering Chemistry Research, 2016, 55(14): 3909–3919
61. Yang S C, Su W N, Rick J, Lin S D, Liu J Y, Pan C J, Lee J F, Hwang B J. Oxygen vacancy engineering of cerium oxides for carbon dioxide capture and reduction. ChemSusChem, 2013, 6(8): 1326–1329
62. Li M, Tumuluri U, Wu Z, Dai S. Effect of dopants on the adsorption of carbon dioxide on ceria surfaces. ChemSusChem, 2015, 8(21): 3651–3660
63. Davydov A A. Basic sites on the surface of oxide catalysts responsible for oxidative methane coupling. Chemical Engineering & Technology, 1995, 18(1): 7–11
64. Daturi M, Binet C, Lavalley J C, Blanchard G. Surface FTIR investigations on $Ce_xZr_{1-x}O_2$ system. Surface and Interface Analysis, 2000, 30(1): 273–277
65. Dong W S, Roh H S, Jun K W, Park S E, Oh Y S. Methane reforming over Ni/Ce-ZrO_2 catalysts: effect of nickel content. Applied Catalysis A, General, 2002, 226(1-2): 63–72
66. Ocampo F, Louis B, Kiwi Minsker L, Roger A C. Effect of Ce/Zr composition and noble metal promotion on nickel based $Ce_xZr_{1-x}O_2$ catalysts for carbon dioxide methanation. Applied Catalysis A, General, 2011, 392(1-2): 36–44
67. Jeon K W, Shim J O, Jang W J, Lee D W, Na H S, Kim H M, Lee Y L, Yoo S Y, Roh H S, Jeon B H, Bae J W, Ko C H. Effect of calcination temperature on the association between free NiO species and catalytic activity of Ni-$Ce_{0.6}Zr_{0.4}O_2$ deoxygenation catalysts for biodiesel production. Renewable Energy, 2019, 131: 144–151
68. Sharma V, Crozier P A, Sharma R, Adams J B. Direct observation of hydrogen spillover in Ni-loaded Pr-doped ceria. Catalysis Today, 2012, 180(1): 2–8
69. Czekaj I, Loviat F, Raimondi F, Wambach J, Biollaz S, Wokaun A. Characterization of surface processes at the Ni-based catalyst during the methanation of biomass-derived synthesis gas: X-ray photoelectron spectroscopy. Applied Catalysis A, General, 2007, 329: 68–78
70. Znak L, Stolecki K, Zieliński J. The effect of cerium, lanthanum and zirconium on nickel/alumina catalysts for the hydrogenation of carbon oxides. Catalysis Today, 2005, 101(2): 65–71
71. Aldana P A U, Ocampo F, Kobl K, Louis B, Thibault-Starzyk F, Daturi M, Bazin P, Thomas S, Roger A C. Catalytic CO_2 valorization into CH_4 on Ni-based ceria-zirconia. Reaction mechanism by operando IR spectroscopy. Catalysis Today, 2013, 215: 201–207
72. Muroyama H, Tsuda Y, Asakoshi T, Masitah H, Okanishi T, Matsui T, Eguchi K. Carbon dioxide methanation over Ni catalysts supported on various metal oxides. Journal of Catalysis, 2016, 343: 178–184
73. Meng F, Li X, Lv X, Li Z. CO hydrogenation combined with water-gas-shift reaction for synthetic natural gas production: a thermodynamic and experimental study. International Journal of Coal Science & Technology, 2018, 5(4): 439–451
74. Barrio L, Kubacka A, Zhou G, Estrella M, Martínez Arias A,

Hanson J C, Fernández García M, Rodriguez J A. Unusual physical and chemical properties of Ni in $Ce_{1-x}Ni_xO_{2-y}$ oxides: structural characterization and catalytic activity for the water gas shift reaction. Journal of Physical Chemistry C, 2010, 114(29): 12689–12697

75. Alamolhoda S, Vitale G, Hassan A, Nassar N N, Almao P P. synergetic effects of cerium and nickel in Ce-Ni-MFI catalysts on low-temperature water-gas shift reaction. Fuel, 2019, 237: 361–372
76. Talkhoncheh S K, Haghighi M. Syngas production via dry reforming of methane over Ni-based nanocatalyst over various supports of clinoptilolite, ceria and alumina. Journal of Natural Gas Science and Engineering, 2015, 23: 16–25
77. Ay H, Üner D. Dry reforming of methane over CeO_2 supported Ni, Co and Ni-Co catalysts. Applied Catalysis B: Environmental, 2015, 179: 128–138
78. Yan X, Liu Y, Zhao B, Wang Z, Wang Y, Liu C J. Methanation over Ni/SiO_2: effect of the catalyst preparation methodologies. International Journal of Hydrogen Energy, 2013, 38(5): 2283–2291
79. Mondal T, Pant K K, Dalai A K. Catalytic oxidative steam reforming of bio-ethanol for hydrogen production over Rh-promoted Ni/CeO_2-ZrO_2 catalyst. International Journal of Hydrogen Energy, 2015, 40(6): 2529–2544